

Spherical Accretion with Anisotropic Thermal Conduction

P. Sharma^{1*}, E. Quataert¹, J. M. Stone²

¹*Astronomy Department and Theoretical Astrophysics Center, 601 Campbell Hall, University of California, Berkeley CA, 94720, USA*

²*Department of Astrophysical Sciences, Peyton Hall, Ivy Lane, Princeton, NJ, 08544, USA*

Accepted . Received ; in original form

ABSTRACT

We study the effects of anisotropic thermal conduction on magnetized spherical accretion flows using global axisymmetric MHD simulations. In low collisionality plasmas, the Bondi spherical accretion solution is unstable to the magnetothermal instability (MTI). The MTI grows rapidly at large radii where the inflow is subsonic. For a weak initial field, the MTI saturates by creating a primarily radial magnetic field, i.e., by aligning the field lines with the background temperature gradient. The saturation is quasilinear in the sense that the magnetic field is amplified by a factor of $\sim 10 - 30$ independent of the initial field strength (for weak fields). In the saturated state, the conductive heat flux is much larger than the convective heat flux, and is comparable to the field-free (Spitzer) value (since the field lines are largely radial). The MTI by itself does not appreciably change the accretion rate \dot{M} relative to the Bondi rate \dot{M}_B . However, the radial field lines created by the MTI are amplified by flux freezing as the plasma flows in to small radii. Oppositely directed field lines are brought together by the converging inflow, leading to significant resistive heating. When the magnetic energy density is comparable to the gravitational potential energy density, the plasma is heated to roughly the virial temperature; the mean inflow is highly subsonic; most of the energy released by accretion is transported to large radii by thermal conduction; and the accretion rate $\dot{M} \ll \dot{M}_B$. The predominantly radial magnetic field created by the MTI at large radii in spherical accretion flows may account for the stable Faraday rotation measure towards Sgr A* in the Galactic Center.

Key words: convection, conduction – magnetic fields, MHD – methods: numerical

1 INTRODUCTION

In magnetized plasmas with a collisional mean free path much greater than the Larmor radius, there is appreciable heat and momentum transport along magnetic field lines but negligible transport across the field lines (Braginskii 1965). Balbus (2000) found that anisotropic thermal conduction fundamentally alters the convective stability of dilute stratified plasmas. For a highly collisional fluid, convection sets in when the entropy increases in the direction of gravity. A low collisionality plasma, however, is unstable to convective-like motions regardless of the sign of the temperature gradient (Balbus 2000; Quataert 2008). For a temperature increasing in the direction of gravity, horizontal fields are the most unstable (the magnetothermal instability; MTI), while when the temperature decreases in the direction of gravity, vertical fields are the most unstable (the heat flux driven buoyancy instability; HBI). The MTI & HBI have been studied us-

ing local simulations by Parrish & Stone (2005, 2007) and Parrish & Quataert (2008), respectively.

In this paper, we study the effects of anisotropic thermal conduction and the MTI on the global dynamics of spherical accretion flows using axisymmetric magnetohydrodynamic (MHD) simulations. Thermal conduction is particularly important for hot low density plasmas in which the electron mean free path is an appreciable fraction of the size of the system, as in, e.g., the accretion flow onto Sgr A* in our Galactic Center and accretion flows onto massive black holes in elliptical galaxies (Tanaka & Menou 2006).

There are several motivations for studying anisotropic conduction in spherical accretion flows. First, the MTI is predicted to be present at large radii in spherical accretion flows, for $r \sim r_B$ (where $r_B \simeq GM/c_s^2$ is the gravitational sphere of influence of the central object and c_s is the isothermal sound speed of the ambient gas). At these radii, the inflow is subsonic and there is sufficient time for the instability to grow (Balbus 2000). At smaller radii ($r \ll r_B$), the MTI is unlikely to grow significantly because the inflow is

* E-mail: psharma@astro.berkeley.edu

supersonic (at least according to the classic Bondi 1952 solution). However, if there is resistive dissipation of the magnetic energy at small radii, conduction may nonetheless be dynamically important because it provides an efficient way to transport energy to larger radii, which can suppress the accretion rate onto the central object (Johnson & Quataert 2007). As we discuss in more detail later in the paper, reduction of accretion rate does not specifically require anisotropic heat transport, but is in fact analogous to the suppression of accretion by magnetic dissipation seen in the resistive MHD simulations of Igumenshchev & Narayan (2002).

A direct observational motivation for studying the MTI in spherical accretion flows is provided by mm observations of Sgr A*. These find a rotation measure (RM) of $\simeq -6 \times 10^5$ rad m⁻² that has been roughly constant since it was first measured over ~ 8 years ago (Aitken et al. 2000; Bower et al. 2005; Marrone et al. 2007). The stability of the observed RM is difficult to explain if the RM is produced by the accretion flow at small radii (Sharma, Quataert, & Stone 2007). In local simulations of the MTI, the field is amplified by factors of $\sim 10 - 30$ and becomes aligned with the temperature gradient (Parrish & Stone 2007). Thus the MTI at large radii in spherical accretion flows is expected to produce a primarily radial magnetic field that could help explain the stable measured RM towards Sgr A* (a possibility we speculated on in Sharma, Quataert, & Stone 2007).

The remainder of this paper is organized as follows. We describe our numerical set up in §2. Because it is not computationally feasible to directly simulate both the small radii close to the central object where most of the gravitationally potential energy is released and the radii $\sim r_B$ where the MTI develops, we carry out two different sets of simulations in this paper, covering different radial scales in the accretion flow. In §3 we present the results of simulations at $r \sim r_B$ that study the development of the MTI for weak initial magnetic fields (see Table 1). In §4 we describe simulations at $r \ll r_B$ that study the effect of thermal conduction and magnetic dissipation on spherical accretion for reasonably strong initial magnetic fields (see Table 2). We then conclude and discuss the astrophysical implications of our results (§5). Throughout this paper we consider the simplified problem of purely spherical accretion; in future studies, we will examine the effects of anisotropic thermal conduction and the MTI in rotating accretion flows.

2 NUMERICAL SIMULATIONS

We use the axisymmetric ZEUS-2D MHD code in spherical geometry (Stone & Norman 1992a,b). We solve the MHD equations with anisotropic thermal conduction:

$$\frac{\partial \rho}{\partial t} + \nabla \cdot (\rho \mathbf{V}) = 0, \quad (1)$$

$$\frac{\partial \mathbf{V}}{\partial t} + \mathbf{V} \cdot \nabla \mathbf{V} = -\frac{\nabla(p + \Pi)}{\rho} + \frac{\mathbf{J} \times \mathbf{B}}{\rho} - \nabla \Phi, \quad (2)$$

$$\frac{\partial \mathbf{B}}{\partial t} = \nabla \times (\mathbf{V} \times \mathbf{B} - \eta \mathbf{J}), \quad (3)$$

$$\frac{\partial e}{\partial t} + \nabla \cdot (e \mathbf{V}) = -(p + \Pi) \nabla \cdot \mathbf{V} - \nabla \cdot \mathbf{Q} + \eta J^2, \quad (4)$$

$$\mathbf{Q} = -\chi \hat{\mathbf{b}} (\hat{\mathbf{b}} \cdot \nabla) T, \quad (5)$$

where ρ is the mass density, \mathbf{V} is the fluid velocity, p is the pressure, Π is an explicit artificial viscosity (e.g., see Stone & Norman 1992a), $\mathbf{J} = c(\nabla \times \mathbf{B})/4\pi$ is the current density, $\Phi = -GM/(r - r_g)$ is the gravitational potential due to a central mass M (we use the pseudo-Newtonian potential of Paczynski & Wiita 1980), $r_g = 2GM/c^2$, \mathbf{B} is the magnetic field strength, η is the explicit resistivity used in some of our simulations, $e = p/(\gamma - 1)$ is the internal energy density (γ is the adiabatic index), \mathbf{Q} is the heat flux along field lines, χ is the thermal diffusivity, $\hat{\mathbf{b}}$ is the unit vector along \mathbf{B} , and T is the temperature. For convenience we often use $\kappa = \chi T/p$ which has the dimensions of a diffusion coefficient (cm² s⁻¹). Anisotropic thermal conduction is added in an operator split fashion with subcycling (e.g., see Parrish & Stone 2005) and is implemented using the method based on limiters that guarantees that heat flows from hot to cold regions (see Sharma & Hammett 2007).

We initialize our simulations using the hydrodynamic Bondi solution with a constant vertical magnetic field B_z . Note that the initial density and temperature gradients are in the radial direction; thus, the initial field is not everywhere perpendicular to the initial temperature gradient, unlike in previous local studies of the MTI. We consider both weak and strong fields to test the effect of the strength of the field on the flow dynamics. The field strength is specified by the dimensionless number B_0 , defined by $B_0 = B_z/(8\pi GM \rho_{\text{out}}/r_{\text{out}})^{1/2}$, where r_{out} is the outer radius of the computational domain and $\rho_{\text{out}} = \rho(r_{\text{out}})$. This is equivalent to $\beta(r_{\text{out}}) = B_0^{-2} [c_s^2/GM/r]_{r_{\text{out}}}$, where β is the ratio of gas pressure to magnetic pressure.

We use an adiabatic index $\gamma = 1.5$ so that the initial solution has a sonic point that lies within the computational domain for our simulations at $r \sim r_B$ (Table 1).¹ For our simulations at large radii, we use the Bondi radius, $r_B = GM/c_s^2$, to normalize length scales in the problem, while for the simulations at small radii, we use the gravitational radius of the central object, $r_g = 2GM/c^2$. We express time in units of inverse rotation frequency at the outer radius of the domain, $\Omega_{\text{out}}^{-1} = (r_{\text{out}}^3/GM)^{1/2}$.

The simulations at $\sim r_B$ described in §3 (Table 1) go from $r_{\text{in}} = 0.04r_B = 2 \times 10^4 r_g$ to $r_{\text{out}} = 16r_B = 8 \times 10^6 r_g$. For these simulations, we keep the temperature at the outer radial boundary fixed at its initial value of $c_s^2/c^2 = 10^{-6}$, i.e., $T_\infty \simeq 10^7$ K. The simulations described in §4 (Table 2) go from $2r_g$ to $256r_g$. The temperature is fixed at the virial temperature $kT_{\text{vir}}/m_p \equiv GMm_p/r$ at the outer boundary (except for one simulation with a very weak initial magnetic field [S2]; in this simulation there is no significant change in the flow properties relative to the hydrodynamic Bondi solution, so fixing the temperature to be that of the initial Bondi solution is more physical). For the simulations at $\sim r_B$ (§3), fixing the temperature at the outer boundary is reasonable because of the large thermal inertia of the plasma at large radii. For the simulations from $2r_g$ to $256r_g$

¹ For $\gamma = 5/3$ the sonic point lies very close to the origin. It is, however, numerically desirable to have the sonic point within the computational domain so that the inner boundary conditions do not influence the solution. We have verified that we get similar results for a run with $\gamma = 5/3$, but with rest of the parameters same as the fiducial run R1.

Table 1. Simulation parameters for runs with $r \sim r_B$ (§3)

Name	Resolution	α_c^\dagger	B_0^\ddagger
R1 ^a	60 × 44	0.2	4.5×10^{-4}
R2	60 × 44	0.2	4.5×10^{-5}
R3	60 × 44	0.2	1.34
D1	120 × 88	0.2	4.5×10^{-4}
D2	120 × 88	0.2	4.5×10^{-5}
Q1	240 × 176	0.2	4.5×10^{-4}
MHD1	60 × 44	0	4.5×10^{-4}
MHD2	60 × 44	0	1.34

$$r_{\text{in}} = 0.04r_B, r_{\text{out}} = 16r_B$$

No explicit resistivity is used for these simulations.

^a This is our fiducial MTI simulation.

[†] The conductivity is defined by $\kappa(r) \equiv \alpha_c(GMr)^{1/2}$ (see §2.1).

[‡] B_0 is the dimensionless magnetic field strength, given by $B_0 = B_z/(8\pi GM\rho_{\text{out}}/r_{\text{out}})^{1/2}$.

Table 2. Simulation parameters for runs with $r \ll r_B$ (§4)

Name	Resolution	α_c^\dagger	B_0^\ddagger	$\frac{\dot{M}_{\text{in}}^*}{\dot{M}_B}$
S1	60 × 44	0.2	0.32	0.01
S2	60 × 44	0.2	10^{-13}	0.52
S3	60 × 44	2	0.32	0.009
S4	60 × 44	20	0.32	0.039
MHD3	60 × 44	0	0.32	0.028

$$r_{\text{in}} = 2r_g, r_{\text{out}} = 256r_g$$

An explicit resistivity is used for these simulations (eq. [6]).

[†] The conductivity is defined by $\kappa(r) \equiv \alpha_c(GMr)^{1/2}$ (see §2.1).

[‡] B_0 is the dimensionless magnetic field strength, given by $B_0 = B_z/(8\pi GM\rho_{\text{out}}/r_{\text{out}})^{1/2}$.

* time averaged accretion rate through r_{in} .

described in §4, however, the choice of the outer temperature boundary condition is more subtle and has a nontrivial effect on the solution. Because we initialize the flow with a $\gamma = 1.5 < 5/3$ solution, the initial temperature is significantly less than the virial temperature. Fixing T_{out} to its initial value is inappropriate because dissipation leads to a temperature $\sim T_{\text{vir}}$ throughout most of the domain and thus setting T_{out} equal to its initial value leads to an unphysically large temperature gradient at r_{out} . Setting $dT/dr = 0$ is unphysical because this sets the heat flux to 0. An alternative boundary condition that we considered, setting a constant heat flux across the outer boundary (corresponding to $dT/dr \approx \text{constant}$), led to a roughly constant temperature throughout the domain with $T_{\text{out}} \simeq T_{\text{in}} \gg T_{\text{vir}}$ after several Ω_{out}^{-1} ; this drove all the mass out of the simulation domain. We thus settled on the physically motivated outer boundary condition of $T_{\text{out}} = T_{\text{vir}}$. Factor of few variations in the exact value of T_{out} did not significantly change the results of the simulations. In both sets of simulations, inflow/outflow boundary conditions are applied at the radial boundaries.

The radial grid is logarithmically spaced (grid spacing $dr \propto r$) so that the number of grid points from r_{in} to $(r_{\text{in}}r_{\text{out}})^{1/2}$ is roughly the same as the number of grid points from $(r_{\text{in}}r_{\text{out}})^{1/2}$ to r_{out} . A logarithmic grid gives reasonable resolution at all radii; e.g., for our simulations at small radii

($2 - 256 r_g$), the cell size at the smallest radii is $\approx 0.2r_g$. A uniform polar grid extends from $\theta = 0$ to $\theta = \pi$. Reflective boundary conditions are applied at the poles. Our standard resolution is 60×44 , but we have also carried out simulations at higher resolution to assess convergence. Our calculations use a version of ZEUS that is not parallel, so that even these modest 2D calculations are time intensive.

We do not use an explicit resistivity for the $r \gtrsim r_B$ simulations in §3 (Table 1). These simulations are primarily aimed at studying the MTI for weak fields in which case the magnetic energy is so small that using an explicit resistivity is not required to correctly capture the dynamics (in addition, we have verified that using the explicit resistivity below does not change the results). However, for $r \ll r_B$ (§4; see Table 2), the gravitational potential energy of the inflowing plasma is converted into magnetic energy by flux freezing. The inflow brings together oppositely directed field lines, which leads to magnetic dissipation and plasma heating. This energy is then transported to large radii by thermal conduction. To capture this dynamics, it is important to conserve energy as accurately as possible. Although we are not using a conservative code, we can capture a reasonable fraction of the dissipated magnetic energy using an explicit resistivity of the form (Stone & Pringle 2001; Igumenshchev & Narayan 2002)

$$\eta = \eta_0 dr^2 \frac{|\nabla \times B|}{\sqrt{4\pi\rho}} \quad (6)$$

with $\eta_0 = 0.15$ (with this choice for η , we find that total energy is conserved to better than 30 % in our simulations at $r \ll r_B$). The resistive terms in the induction and internal energy equations are included using the method of Fleming, Stone, & Hawley (2000).

Although our simulations are two-dimensional, the turbulent magnetic and velocity fields do not decay at late times, because the anti-dynamo theorem does not apply when a net magnetic flux threads the simulations domain. In this case the source current for the magnetic field is outside of the simulation domain (Balbus & Hawley 1998).

2.1 Thermal Conductivity

In a collisional plasma, the thermal conductivity is given by $\kappa \simeq 4.3 \times 10^9 T^{5/2} / n \text{ cm}^2 \text{ s}^{-1}$ (Spitzer 1962). However, the inner regions of hot accretion flows are, in many cases, collisionless with the electron mean free path due to Coulomb collisions larger than the radius (e.g., Tanaka & Menou 2006; Sharma et al. 2007); the collisional result is thus inapplicable. In a collisionless plasma, electrons can in principle carry a free streaming heat flux as large as $Q \sim nkTv_e \sim 40\rho v_i^3$ ($v_{i,e} = [kT/m_{i,e}]^{1/2}$ is the thermal speed; Cowie & McKee 1977; Snyder, Hammett, & Dorland 1997). The diffusion coefficient in this case is $\kappa \sim v_e r \propto r^{1/2}$, assuming a virial temperature proportional to r^{-1} . Motivated by the application to collisionless systems such as Sgr A*, we take $\kappa \propto r^{1/2}$ as the thermal conductivity for our simulations and define the dimensionless conductivity α_c by

$$\kappa \equiv \alpha_c(GMr)^{1/2}. \quad (7)$$

Although the scaling $\kappa \sim v_e r \propto r^{1/2}$ is well-motivated, the precise value of α_c is difficult to calculate. It depends on the

electron mean free path in the collisionless limit, which is determined by the rate of pitch angle scattering by small-scale (high frequency) turbulent fluctuations. Motivated by the results of Sharma et al. (2006) and Sharma et al. (2007) on pitch angle scattering in collisionless accretion flows, we take $\alpha_c \simeq 0.2 - 2$, i.e., $\kappa = (0.2 - 2)(GMr)^{1/2}$, as our fiducial diffusion coefficient. This value is much smaller than the maximum free-streaming thermal conductivity that could be obtained if the electrons are virial. Our choice for $\kappa(r)$ is such that the large-scale thermal conduction timescale ($t_{\text{cond}} = r^2/\kappa$) is comparable to the free-fall timescale ($t_{\text{ff}} = [2GM/r^3]^{-1/2}$). Thermal conduction can thus lead to a significant modification of the thermal structure of the plasma (as we shall see). Since both t_{cond} and t_{ff} scale as $r^{3/2}$, this is true at all radii. In addition, with $t_{\text{cond}} \sim t_{\text{ff}}$ on large scales, small-scale perturbations are effectively isothermal and the MTI grows at its maximal rate (Balbus 2000). For the MTI simulations at $\sim r_B$, we carried out simulations with α_c factors of few smaller and larger than our fiducial choice of $\alpha_c = 0.2$, and found results essentially identical to those described here. For the simulations at $r \sim 2 - 200r_g$, resistive heating and thermal conduction significantly modify the dynamical properties of the accretion flow; in this case, we show solutions for a variety of values of α_c to explicitly show the dependence on the conductivity (which is still relatively modest).

As we discuss in §3, it turns out that a conductivity $\kappa \propto r^{1/2}$ has the property that $\nabla \cdot \mathbf{Q} \simeq 0$ for the *initial* Bondi solution near $r \sim r_B$. Since the initial condition is already approximately a steady state solution even in the presence of conduction (modulo the MTI), including conductivity does not affect the structure of the plasma. We thus carried out simulations at $\sim r_B$ with other choices for $\kappa(r)$ (namely, $\kappa \propto r^{3/2}$ and $\kappa \propto r^{-1/2}$). Although we do not show detailed results for these simulations, in all cases we found that the MTI rapidly creates radial magnetic field lines and that conduction along the radial magnetic field lines forces the density and temperature structure of the plasma to readjust in order to satisfy $\nabla \cdot \mathbf{Q} \simeq 0$. This can lead to modest modifications in the density and temperature profiles of the flow, but in all cases the accretion rate \dot{M} was within a factor of a few of the Bondi rate.

3 SIMULATIONS AT $R \sim R_B$

Figure 1 shows several different timescales characterizing the initial Bondi solution. For $r \gtrsim r_B$ the infall timescale (t_{in}) is much longer than the timescale for the MTI to grow (t_{MTI}) and the instability grows exponentially. The MTI can thus saturate before the plasma flows in. At smaller radii ($r \lesssim r_B$), however, where the inflow time is comparable to the MTI growth time, the growth is algebraic and the MTI is less likely to have a significant effect on the dynamics. Instead, at $r \ll r_B$, the magnetic field will be primarily amplified by flux freezing. Here we discuss our simulations of the MTI at $r \sim r_B$. In the next section we present the results of simulations at $r \ll r_B$.

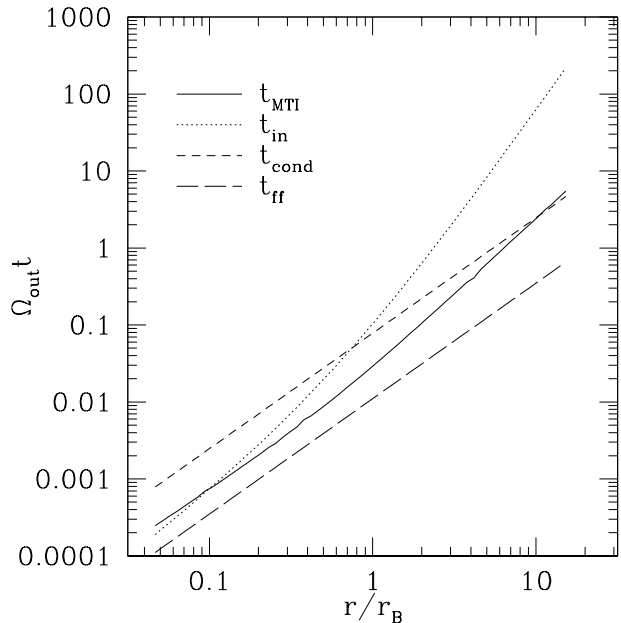


Figure 1. Various timescales (in units of $\Omega_{\text{out}}^{-1} = [GM/r_{\text{out}}^3]^{-1/2}$) as a function of radius for the initial Bondi solution: the MTI growth time $t_{\text{MTI}} = \gamma_{\text{MTI}}^{-1}$ (the maximum MTI growth rate is given by $\gamma_{\text{MTI}}^2 = [1/\rho][dp/dr][d \ln T/dr]$), $t_{\text{in}} = r/V_r$ (the local infall timescale), $t_{\text{cond}} = r^2/\kappa$ (the large scale thermal diffusion timescale for $\alpha_c = 0.2$), and $t_{\text{ff}} = (r^3/2GM)^{1/2}$ (the local free-fall timescale). The infall timescale is much longer than the timescale for the growth of the MTI for $r \gtrsim r_B$; thus the MTI rapidly modifies the magnetic field structure.

3.1 The Fiducial MTI Simulation

Our fiducial simulation (labeled “R1”) uses $\kappa(r) = 0.2(GMr)^{1/2}$ and has an initial magnetic field strength of $B_0 = 4.5 \times 10^{-4}$, corresponding to $\beta \simeq 10^8$ at r_{out} . This simulation describes the evolution of the MTI for weak magnetic fields. We choose the lower resolution simulation R1 as our fiducial case because it finishes relatively quickly (in \lesssim a week); this enables us to readily study the effects of different boundary conditions, different choices for the thermal conductivity, etc. We also present higher resolution calculations (e.g., D1 & Q1, which take several months to finish) that are similar to R1, although with a modest increase in the field amplification by the MTI (see Fig. [9]).

Figure 2 shows the r and θ components of the magnetic energy density as a function of time for the fiducial simulation and for an MHD simulation without conduction, but with the same initial conditions. The energy is averaged from $r = r_{\text{out}}/10$ to r_{out} , to isolate the radii where $t_{\text{in}} \gg t_{\text{MTI}}$ (see Fig. 1) and the instability is unaffected by inflow. The top panel in Figure 2 shows the early linear growth of the MTI, while the bottom panel shows the longer time evolution. Because we are averaging over a range of radii, there is no unique growth rate for the MTI, but the maximal MTI growth rate evaluated at $r \simeq r_{\text{out}}/3$ provides a reasonable fit to the early time growth (long-dashed line). After a few free-fall times (several MTI growth times; see Fig. 1), the magnetic field ceases to grow exponentially and the growth becomes algebraic. This represents the saturation of

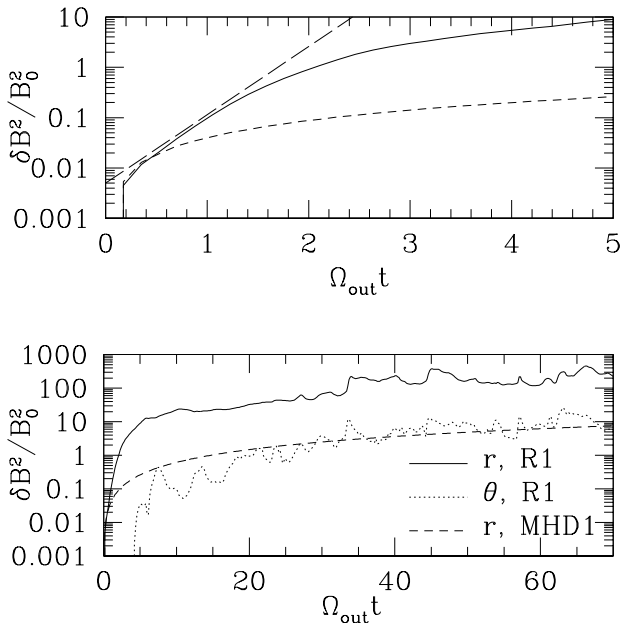


Figure 2. Change in volume averaged magnetic energy (radial and θ components normalized to the initial magnetic energy) in a shell from $r_{\text{out}}/10$ to r_{out} as a function of time. The top panel shows the early-time evolution of δB_r^2 (solid line) for the fiducial MTI simulation (R1) compared to δB_r^2 for an MHD simulation with the same initial conditions (MHD1; short-dashed line). The long-dashed line indicates the growth rate of the MTI at $r \simeq r_{\text{out}}/3$. The bottom panel shows the same field components over longer timescales, along with δB_θ^2 (dotted line) for the fiducial run. $\delta B_{r,\theta}^2 \equiv \langle (B_{r,\theta}^2)_V - B_{r,\theta,0}^2 \rangle$, where $\langle \rangle_V$ denotes volume average and B_0 is the initial field strength.

the MTI; the later growth of the field is due to flux freezing. This can be seen explicitly by noting that the MHD simulation (short-dashed line) shows the same algebraic growth in the magnetic field with time, only at a reduced magnitude of \mathbf{B} because there is no early MTI growth. Note that the net increase in magnetic energy because of the MTI is quite modest: $\beta \gg 1$ even in the saturated state.

Figure 3 compares the plasma β at the end ($\Omega_{\text{out}} t \simeq 60$) of the fiducial run and the corresponding MHD simulation. The magnetic field unit vectors are also shown. The plasma β with conduction is a factor of ~ 100 smaller than without conduction (as is also seen in Fig. 2), indicating that the MTI alone amplifies the field by a factor of ~ 10 . Since the simulations do not run for even one infall timescale at r_{out} , the magnetic field lines at large radii do not change significantly in the MHD simulation and remain primarily vertical. By contrast, the magnetic field is completely restructured in the presence of anisotropic conduction because of the MTI. The magnetic field at the end of the simulation is primarily radial. This can also be seen in Figure 4, which shows the volume averaged angle of the magnetic field with respect to the radial direction as a function of time for several runs. In the linear stage of the MTI, the radial field is amplified exponentially; after saturation, the field direction, although turbulent, continues to become radial because of flux freezing (as also occurs in the pure MHD simulation shown in Fig. 4), although this occurs on the slower inflow timescale.

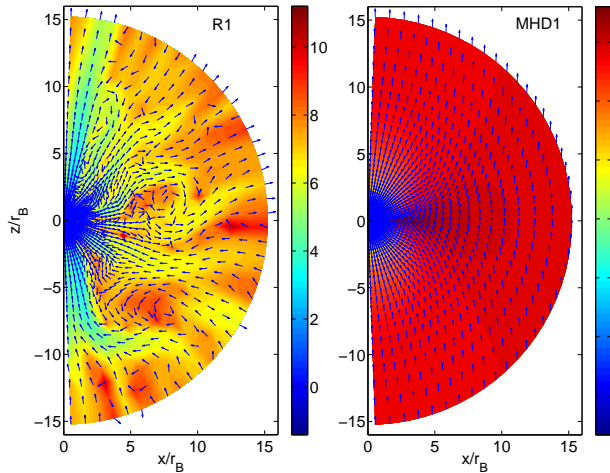


Figure 3. \log_{10} of plasma β ($\equiv 8\pi p/B^2$) at the end ($\Omega_{\text{out}} t \approx 60$) of the fiducial MTI run R1 (left), and at the end of the MHD simulation MHD1 (right). Also shown are arrows indicating the local magnetic field direction. The magnetic field is turbulent but primarily radial in the presence of anisotropic conduction. In MHD, the field remains primarily vertical at large radii, because flux freezing only reorients the field on the (slow) inflow timescale.

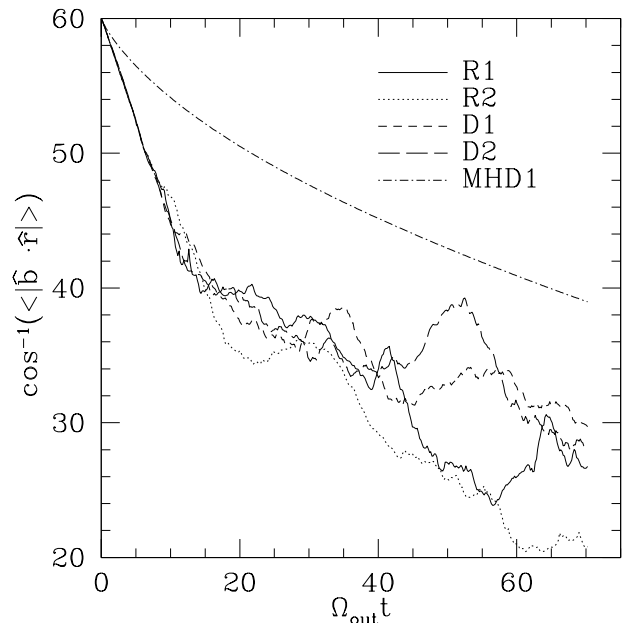


Figure 4. Volume averaged angle (in degrees) of the magnetic field lines with respect to the radial direction as a function of time for different runs (the average is from $r_{\text{out}}/10$ to r_{out} , as in Fig. 2).

Our conclusion that the MTI generates primarily radial field lines in the saturated state is fully consistent with the local MTI simulations of Parrish & Stone (2005, 2007).

To understand the saturation of the MTI, it is useful to consider the linear dynamics of the instability. In the WKB limit, and assuming rapid conduction and weak magnetic

fields, the linear growth rate is given by (Quataert 2008)

$$\gamma^2 \approx \frac{1}{\rho} \frac{dp}{dr} \left(\frac{d \ln T}{dr} \right) \left[(1 - 2b_r^2) \frac{k_\theta^2}{k^2} + \frac{2b_\theta b_r k_\theta k_r}{k^2} \right], \quad (8)$$

where k_r and k_θ are the r and θ wavenumbers, and b_r and b_θ are the r and θ magnetic field unit vectors. Our initial field is vertical with a θ dependent b_r and b_θ . In the saturated state, where $b_r \simeq 1$ and $b_\theta \ll 1$, the fastest growth rate of the MTI is $\gamma \simeq |[1/\rho][dp/dr][d \ln T/dr]|^{1/2} b_\theta$, a factor of $\sim b_\theta$ smaller than the growth rate in the initial configuration. Growth occurs only for modes satisfying $k_\theta/k_r \lesssim 2b_\theta$, i.e., for small radial wavelengths. The significant decrease in the growth rate of the MTI for nearly radial fields qualitatively explains why magnetic field reorientation leads to saturation of the instability. In addition, even if there is growth at late times, it is on small radial scales and so is unlikely to modify the large-scale field structure or magnetic energy. The MTI can also saturate by making $d \ln T/dr \approx 0$, i.e., by making the plasma isothermal. Whether the plasma becomes isothermal or not depends on $\kappa(r)$ (and on the boundary conditions), which influences how the density and temperature adjust to make $\nabla \cdot \mathbf{Q} \simeq 0$ in steady state. Figure 5 shows that for our fiducial simulation, there is very little change in the temperature and density profiles during the simulation. For our choice of $\kappa \propto r^{1/2}$, it turns out that the initial Bondi flow nearly satisfies $\chi r^2 dT/dr = \text{constant}$ near $\sim r_B$. Thus when the MTI reorients the field lines to be primarily radial, little evolution in $\rho(r)$ and $T(r)$ is required to make $\nabla \cdot \mathbf{Q} \simeq 0$. As noted in §2.1, we carried out simulations with different $\kappa(r)$ in order to assess its effects on the flow dynamics (although we believe that the fiducial choice considered here is the most physical for collisionless systems). In all cases, we found that the MTI reorients the field lines to be primarily radial and that $\rho(r)$ and $T(r)$ adjust so that $\nabla \cdot \mathbf{Q} \simeq 0$.

Figure 6 shows the time and angle averaged mass accretion rate in the saturated state as a function of radius. In MHD the velocity is always radial and inwards and the mass accretion rate is equal to the Bondi rate (for this $\beta \gg 1$ simulation). The solid line in Figure 6 shows the net mass accretion rate for the fiducial run, $\dot{M} = 2\pi r^2 \int \rho V_r \sin \theta d\theta$; also shown are the mass fluxes of material with $V_r > 0$ and $V_r < 0$. Although there are MTI-driven convective motions, they are modest and the net accretion rate is only slightly smaller than the Bondi accretion rate. This is partially a consequence of the fact that the density and temperature profiles change very little in the course of the simulation (Fig. 5). However, even for different choices of α_c and $\kappa(r)$, we still found $\dot{M} \sim \dot{M}_B$ for MTI simulations with initially weak fields. The MTI by itself thus does not significantly change the accretion rate onto the central object. This is in contrast to the very strong suppression of \dot{M} found in the next section by the combined action of magnetic dissipation, plasma heating, and thermal conduction at $r \ll r_B$.

Figure 7 shows time and angle averaged luminosities ($4\pi r^2 \times$ energy fluxes) for energy transport by conduction and MTI-initiated convection. The luminosities are normalized to the field free (“Spitzer”) conductive luminosity at r_{out} . The radial conductive luminosity ($4\pi r^2 Q_c$) is roughly constant as a function of radius for $r \gtrsim 0.1 r_B$, as would be expected in steady state. The conductive heat flux is similar to the local field-free value at all radii because the field lines are primarily radial. The non-conductive energy transport

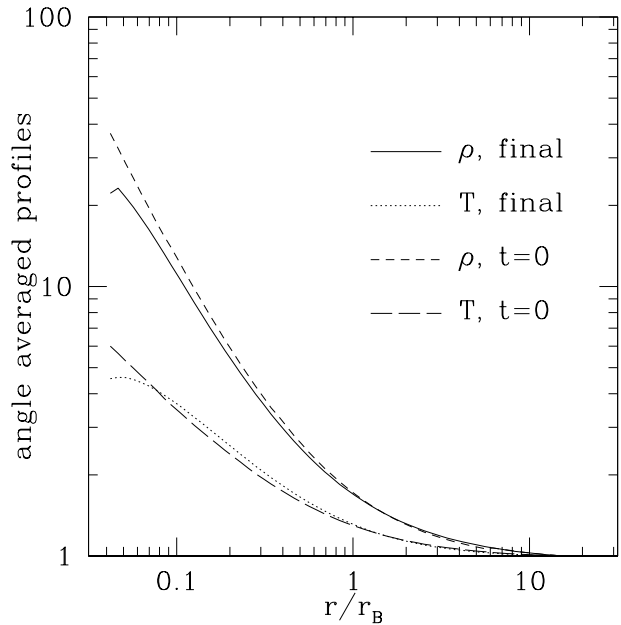


Figure 5. Density (short-dashed line) and temperature (long-dashed line) as a function of radius for the initial Bondi solution; time and angle averaged density (solid line) and temperature (dotted line) at late times as a function of radius for the fiducial MTI simulation R1. Density and temperature are normalized to their values at r_{out} . There is very little change in the radial density and temperature profiles during the simulation.

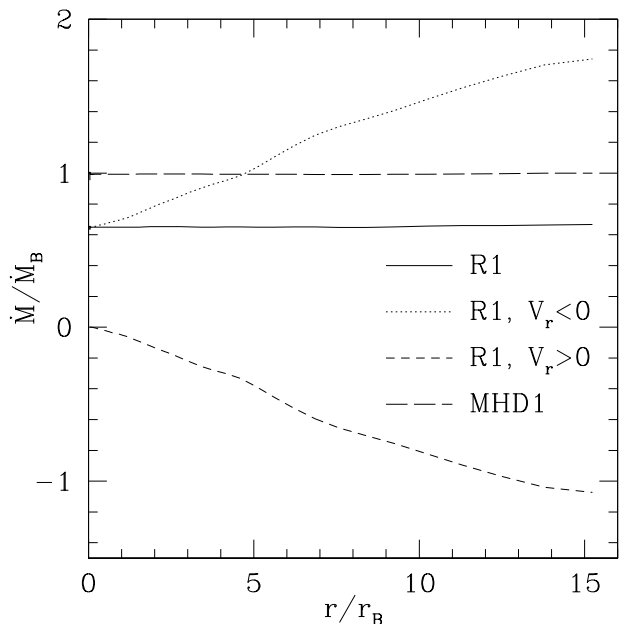


Figure 6. Time and angle averaged mass accretion rate (\dot{M}) in the fiducial MTI simulation R1 at late times, as a function of radius (normalized to the Bondi accretion rate, \dot{M}_B): net mass accretion rate (solid line), mass inflow rate (dotted line; with $V_r < 0$), and mass outflow rate (short-dashed line; with $V_r > 0$). The mass accretion rate in MHD is shown by the long-dashed line.

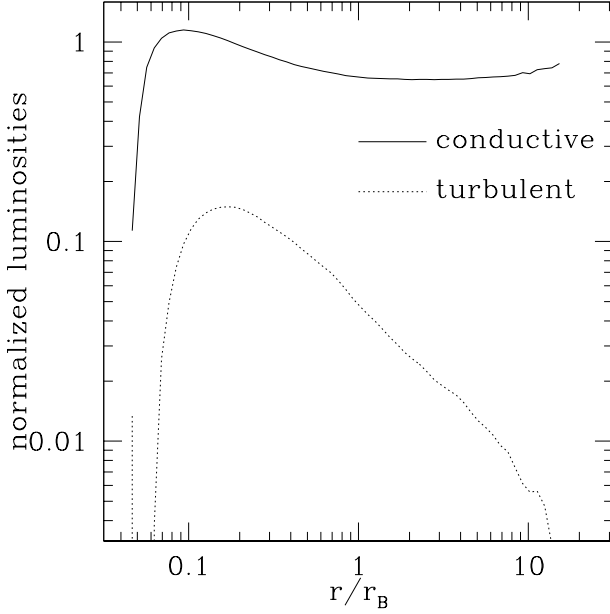


Figure 7. Time and angle averaged conductive (solid line; Q_c) and turbulent (dotted line; Q_t) luminosities ($4\pi r^2 \times$ energy fluxes) as a function of radius for the fiducial MTI simulation R1; see §3.1 for the definition of Q_t . The luminosities are normalized to the field free conduction luminosity at r_{out} .

has contributions from the kinetic energy flux ($\rho V^2 V_r/2$), the enthalpy flux ($\gamma/(\gamma-1)pV_r$), and the Poynting flux. The latter is negligible for the weak magnetic field values considered here. Both the kinetic energy flux and the enthalpy flux can be split up into terms proportional to the mass accretion rate (the advective flux of energy Q_a due to the bulk motion of the fluid) and terms which represent the turbulent/convective transport of energy (Q_t). Mathematically, this can be seen by decomposing the fluid variables into mean and fluctuating components; e.g., the radial velocity is taken to be $V_r = \langle V_r \rangle + \delta V_r$, where $\langle \rangle$ represents an appropriate average and δ represents deviation from the average. For our purposes, the average is taken over θ at each time at a given r . With this decomposition, the average kinetic energy flux is given by

$$\frac{1}{2} \langle \rho V^2 V_r \rangle = Q_{K,a} + Q_{K,t},$$

with

$$Q_{K,a} = \frac{1}{2} \langle \rho V_r \rangle [\langle V_r \rangle^2 + \langle V_\theta \rangle^2 + \langle \delta V_r^2 \rangle + \langle \delta V_\theta^2 \rangle], \quad (9)$$

$$Q_{K,t} = \frac{1}{2} \langle \delta(\rho V_r) (\delta V_r^2 + \delta V_\theta^2) \rangle + \langle \delta(\rho V_r) \delta V_r \rangle \langle V_r \rangle + \langle \delta(\rho V_r) \delta V_\theta \rangle \langle V_\theta \rangle, \quad (10)$$

where $Q_{K,a}$ is the advective flux of kinetic energy and $Q_{K,t}$ is the turbulent/convective kinetic energy flux. Similarly, the average enthalpy flux can be written as

$$\frac{\gamma}{\gamma-1} \langle p V_r \rangle = Q_{e,a} + Q_{e,t},$$

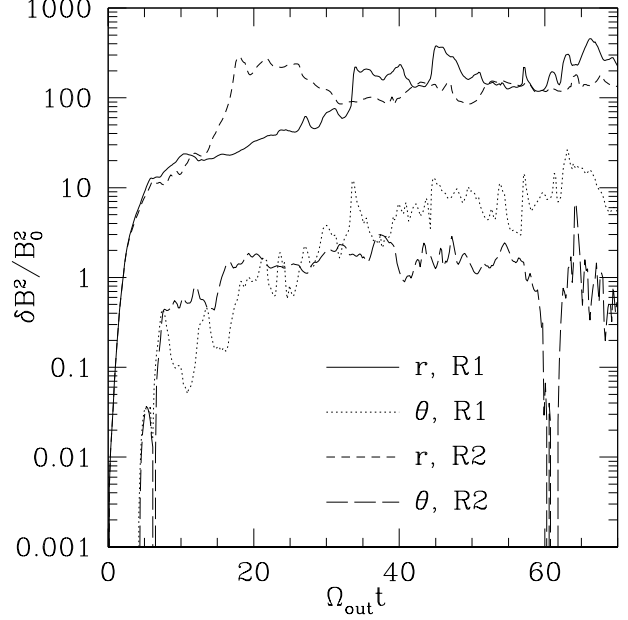


Figure 8. Volume averaged magnetic energy (normalized to the initial magnetic energy) in a shell from $r_{\text{out}}/10$ to r_{out} as a function of time: $\delta B_r^2/B_0^2$ (solid line), $\delta B_\theta^2/B_0^2$ (dotted line) for the fiducial MTI simulation R1; $\delta B_r^2/B_0^2$ (short-dashed line), $\delta B_\theta^2/B_0^2$ (long-dashed line) for R2 (which has an initial field strength B_0 10 times smaller than R1); $\delta B_{r,\theta}^2 = (\langle B_{r,\theta}^2 \rangle_V - B_{r,\theta,0}^2)$, where $\langle \rangle_V$ denotes volume average and B_0 is the initial field strength.

with

$$Q_{e,a} = \frac{\gamma}{\gamma-1} \langle \rho V_r \rangle \langle c_s^2 \rangle, \quad (11)$$

$$Q_{e,t} = \frac{\gamma}{\gamma-1} [\langle V_r \rangle \langle \delta \rho \delta c_s^2 \rangle + \langle \rho \rangle \langle \delta V_r \delta c_s^2 \rangle + \langle \delta \rho \delta V_r \delta c_s^2 \rangle], \quad (12)$$

where $c_s^2 = p/\rho \simeq kT/m_p$. Figure 7 shows the total turbulent energy flux in the MTI simulations at large radii, $Q_t = Q_{e,t} + Q_{K,t}$; the turbulent energy transport – which is dominated by the $\langle \delta V_r \delta c_s^2 \rangle$ term in equation (12) – is much smaller than the conductive energy transport at all radii.

3.2 Effect of B_0

If the MTI saturates by making the magnetic field lines primarily radial, as we showed in the previous section, it is reasonable to expect that the saturation magnetic field strength will scale with the initial magnetic field strength (since a smaller radial field is required to make an initially weaker vertical magnetic field radial). To test this hypothesis we carried out the simulation R2 with a weaker vertical magnetic field ($B_0 = 4.5 \times 10^{-5}$), corresponding to $\beta \simeq 10^{10}$ at r_{out} . All other parameters are same as the fiducial run.

Figure 8 shows the results from run R2 compared to those of R1. The most interesting result is that even nonlinearly $\delta B_{r,\theta}^2/B_0^2$ for R1 and R2 are similar. That is, the late time magnetic energy is roughly proportional to the initial magnetic energy in the domain. This indicates that the saturation of the MTI is quasilinear: for weak magnetic fields,

the MTI saturates when the field lines become radial, which requires a $\delta B \propto B_0$.

We also carried out simulations with much stronger initial magnetic fields, $B_0 = 1.3$, corresponding to $\beta \simeq 10$ at r_{out} (run R3 with conduction and run MHD2 without conduction). The magnetic field is sufficiently strong that the MTI is suppressed by magnetic tension. Indeed, we find that there are only small differences between the simulations with and without conduction. In both cases the magnetic field at small radii is amplified by the converging inflow. Magnetic tension prevents plasma infall in the equatorial region; mass accretion is dominated by the polar regions. There is a strong equator-pole anisotropy because of the strong magnetic field. The polar regions are cold, low density, and magnetically dominated ($\beta \ll 1$), with large radial infall velocities. We find a modest reduction in the accretion rate for these strong-field simulations at $\sim r_B$, with the mass accretion rate through r_{in} being $\simeq 25\%$ of the Bondi rate. Finally, we find that including an explicit resistivity does not have a significant effect on the flow dynamics at large radii even for energetically significant magnetic fields. This is in contrast to the simulations described in §4 in which there is significant magnetic dissipation when $\beta \sim 1$ at $r \ll r_B$. The difference is probably that the supersonic inflow at $r \ll r_B$ is much more effective than the slow inflow velocities at $\sim r_B$ at forcing reconnection/dissipation of field lines.

3.3 Effect of Resolution

To assess the effect of resolution we carried out several higher resolution runs: run D1, which is analogous to the fiducial simulation R1 but with twice the resolution, run D2 which is analogous to R2 but with twice the resolution, and run Q1 which has four times the resolution of R1. While the overall dynamics is very similar to the lower resolution runs, the magnetic energy is a factor of few larger in the higher resolution simulations. Figure 9 compares the fiducial run R1 with D1 and Q1, and shows that both δB_r^2 and δB_θ^2 are larger in higher resolution runs than they are in R1, by a factor of $\simeq 5$. The same is true for D2 compared with R2. In particular, Figure 9 shows that the phase of linear exponential magnetic field amplification occurs for a longer period of time in the higher resolution simulations. Since the late-time magnetic field growth is simply flux freezing of the early-time field, this leads to an enhanced field at all times. The fastest growing MTI modes for approximately radial magnetic fields are those with $2k_r/k_\theta \gtrsim b_\theta^{-1}$, which is a resolution dependent criterion. Higher resolution simulations can thus resolve growth for longer times and to larger radial fields, i.e., to smaller b_θ .

Although the fastest growth of the MTI occurs at small scales, nonlinearly one expects the energy contained in small scales to be subdominant for sufficiently high resolution simulations. Indeed, Figure 9 shows that both the radial and polar magnetic energies are similar for the higher resolution runs D1 and Q1. This indicates that nonlinear saturation of the MTI is reasonably independent of resolution for sufficiently high resolution simulations (e.g., runs D1 and Q1).

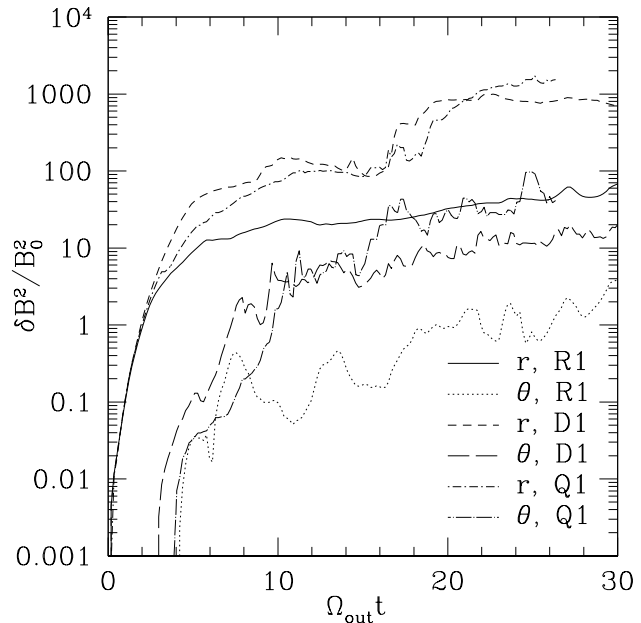


Figure 9. Volume averaged magnetic energy (normalized to the initial magnetic energy) in a shell from $r_{\text{out}}/10$ to r_{out} as a function of time, comparing different resolution runs: $\delta B_r^2/B_0^2$ (solid line), $\delta B_\theta^2/B_0^2$ (dotted line) for the fiducial run R1; $\delta B_r^2/B_0^2$ (short-dashed line), $\delta B_\theta^2/B_0^2$ (long-dashed line) for D1, with twice the resolution as R1; and $\delta B_r^2/B_0^2$ (short dot-dashed line), $\delta B_\theta^2/B_0^2$ (long dot-dashed line) for Q1, with four times the resolution of R1. As before, $\delta B_{r,\theta}^2 = (\langle B_{r,\theta}^2 \rangle_V - B_{r,\theta,0}^2)$, where $\langle \rangle_V$ denotes volume average and B_0 is the initial field strength.

4 SIMULATIONS AT $R \ll R_B$

As shown in the previous section, the MTI generates a radial field at $\sim r_B$ in dilute spherical accretion flows. As the plasma flows in to yet smaller radii, this field will be amplified by flux freezing. It is well known that for inflow according to the Bondi solution (Bondi 1952), the magnetic energy increases more rapidly with decreasing radius than the gravitational energy of the gas, and eventually the field becomes energetically important (e.g., Shvartsman 1971). Igumenshchev & Narayan (2002) showed that when $\beta \sim 1$ magnetic dissipation of the amplified field becomes significant and the dynamics of the inflow changes appreciably. Resistive heating increases the temperature of the plasma and may drive thermal convection. The accretion rate onto the central object decreases by a few orders of magnitude. In this section, we examine the modification to these results caused by anisotropic thermal conduction. Our general conclusion that mass accretion is significantly suppressed is consistent with that of Igumenshchev & Narayan (2002), but we find that the conductive transport of energy is more important than the convective transport.

Our simulations at small radii have $r_{\text{in}} = 2r_g$ and $r_{\text{out}} = 256r_g$; their properties are summarized in Table 2. The initial conditions are chosen from the same Bondi solution used in the previous section. Run S1 takes $\alpha_c = 0.2$ and $B_0 \simeq 0.32$. This value of B_0 corresponds to $\beta \simeq 1$ at r_{out} . Igumenshchev & Narayan (2002) have shown that a weaker field at r_{out} means that significant dissipation does

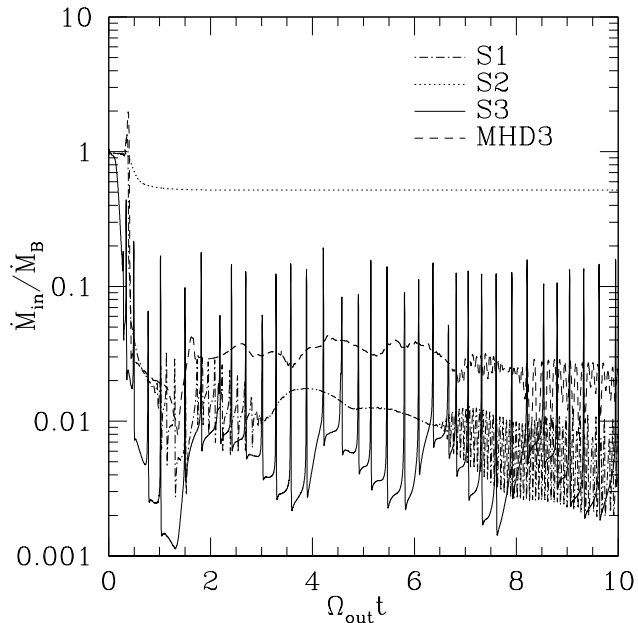


Figure 10. Mass accretion rate (normalized to the initial Bondi rate) at $r_{in} = 2r_g$ as a function of time for runs S1, S2, S3, & MHD3, all listed in Table 2. The mass accretion rate in the presence of strong fields and resistive dissipation is reduced significantly relative to the Bondi rate, irrespective of whether conduction is present. Note that the mass accretion rate for run S3 shows very regular “flares;” these persist even if we vary many of the numerical details of the calculation (see text for details).

not begin until smaller radii (and later times), but that otherwise the results do not depend sensitively on the choice of B_0 . In addition to the fiducial value of $\alpha_c = 0.2$, we also performed simulations with $\alpha_c = 2$ and 20; the latter corresponds roughly to the maximum rate of heat transport by free-streaming electrons. We present results for a variety of α_c but focus on the $\alpha_c = 2$ simulation (S3) because it most clearly demonstrates the relevant physics.

S2 and MHD3 represent control simulations. S2 is a simulation with anisotropic conduction but with a very weak field. As expected, it is effectively a laminar hydrodynamic Bondi solution (see Fig. 14), with no evidence for the MTI or dynamically significant resistive heating. MHD3 is a resistive MHD simulation with $\beta \simeq 1$ at r_{out} , analogous to the simulations performed by Igumenshchev & Narayan (2002).

4.1 Results

Figure 10 shows the mass accretion rate at the inner radius r_{in} as a function of time. The weak-field simulation S2 shows no significant differences relative to the Bondi solution; the factor of $\simeq 2$ decrease in \dot{M} for S2 in Figure 10 is due to the fact that thermal conduction leads to small changes in the density and temperature profiles of the flow. In addition, there is no indication that the MTI is present, unlike in the simulations at large radii discussed in the previous section. By contrast, all of the simulations with $\beta \sim 1$ at r_{out} – both with and without anisotropic conduction – show a significant decrease in \dot{M} after a few free-fall times,

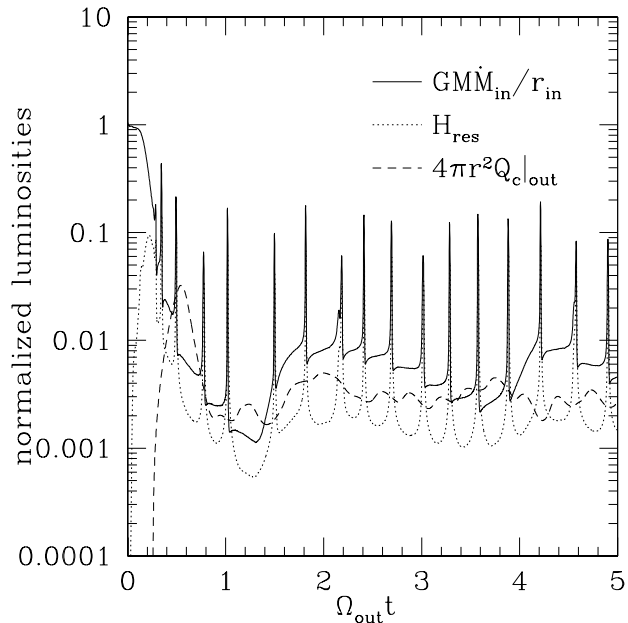


Figure 11. Total energy generation and loss rates (normalized to $G\dot{M}\dot{M}/r_{in}$) as a function of time for run S3 with $\alpha_c = 2$: gravitational energy released by accretion $G\dot{M}\dot{M}/r_{in}$ (solid line), volume integrated resistive heating rate ($H = 2\pi \int dr d\theta r^2 \sin\theta \eta J^2$; dotted line), and conductive luminosity at the outer radius of the domain ($4\pi r^2 Q_c|_{out}$; short-dashed line). Most of the energy released by accretion is captured by our explicit resistivity; this energy is then transported to large radii by conduction.

with $\dot{M} \sim 0.01 - 0.03 \dot{M}_B$ at late times. We focus our interpretation on the simulations with conduction, since our results for simulations without conduction are similar to those presented in Igumenshchev & Narayan (2002). Note that the simulations with anisotropic conduction show episodic “flares” in \dot{M} and other dynamical quantities that are not as prominent in the MHD simulations; these are discussed more below.

Figure 11 shows the overall energetics for the simulation with $\alpha_c = 2$ (S3). A significant fraction of the gravitational potential energy released by the inflowing matter (solid line) is converted into magnetic energy by flux freezing. Resistive dissipation of oppositely directed field lines leads to plasma heating. Although our numerical routine is not conservative, we do have an explicit resistivity and Figure 11 shows that the total resistive heating in the computational domain (dotted line) is similar to the gravitational potential energy released by accretion.² In turn, much of this energy is transported out of the computational domain by conduction, as shown by the short-dashed line in Figure 11, which is the conductive luminosity at the *outer* radius r_{out} . The results for runs S1 & S4 (which have different conductivities α_c) look similar.

² In addition to explicit resistivity – which is the dominant source of heating in our calculations – we also include artificial viscosity for shock capturing. Explicit resistivity, artificial viscosity, and inherent numerical diffusion all lead to increase in entropy in the simulations.

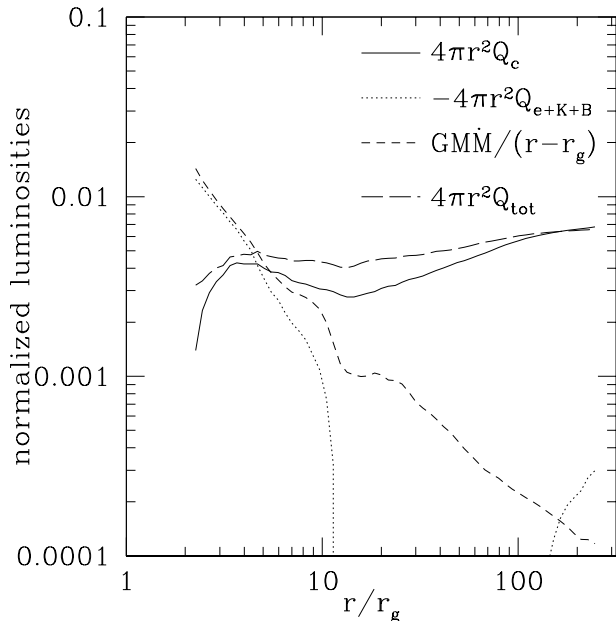


Figure 12. Time and angle averaged luminosities ($4\pi r^2 \times$ energy fluxes, normalized to $G\dot{M}M_B/r_{\text{in}}$) as a function of radius for run S3 ($\alpha_c = 2$): conductive luminosity $4\pi r^2 Q_c$, energy transport by fluid motion $4\pi r^2 Q_{e+K+B}$ (which includes thermal, kinetic, and Poynting contributions), total power generated by accretion ($G\dot{M}M/(r - r_g)$), and the total luminosity ($4\pi r^2 Q_{\text{tot}}$, where $Q_{\text{tot}} = Q_c + Q_{e+K+B} + G\dot{M}M/4\pi[r - r_g]$).

Another indication of the importance of the conductive transport of energy is given in Figure 12, which shows the time averaged luminosities carried by conduction (Q_c) and fluid motion (Q_{e+K+B}) as a function of radius for $\alpha_c = 2$ (S3). Note that here we are comparing the conductive luminosity to the total thermal+kinetic+magnetic transport of energy $Q_{e+K+B} \equiv \rho V^2 V_r / 2 + \gamma p V_r / (\gamma - 1) + [B^2 V_r - (\mathbf{B} \cdot \mathbf{V}) V_r] / 4\pi$ which includes kinetic, thermal, and Poynting contributions; the radial velocity V_r in Q_{e+K+B} is the total radial velocity and thus Q_{e+K+B} includes energy transport by the mean fluid motion and by the turbulence (unlike Q_t in §3 and Fig. 7 which is solely the turbulent transport). The energy carried by conduction is significantly larger than that carried by other mechanisms (in particular, either advection or convection) except at the smallest radii, where the pseudo-Newtonian potential leads to supersonic inflow. In addition, the conductive luminosity is roughly independent of radius, as would be expected in steady state given a source of heating at small radii. These results demonstrate that the gravitational potential energy released at small radii by magnetic dissipation is carried to larger radii by conduction. We find similar results for $\alpha_c = 0.2$ (S1) and $\alpha_c = 20$ (S4), but for larger values of α_c , the conductive energy transport becomes the dominant energy transport mechanism at smaller radii. Only in the limit $\alpha_c \ll 1$ do the simulations with conduction become similar to the simulations of Igumenshchev & Narayan (2002).

Figure 13 shows how the time and angle averaged density and temperature profiles of the accretion flow change in the presence of resistive heating and conduction. The initial

temperature of the flow is much less than the virial temperature $kT_{\text{vir}} \equiv G\dot{M}m_p/r$ because we initialize a Bondi solution with $\gamma = 1.5 < 5/3$. By contrast, both the MHD simulation and the simulations with anisotropic conduction have time-averaged temperatures of $T \sim T_{\text{vir}}$ because much of the accretion energy is thermalized as heat via resistive dissipation. The resulting high temperatures lead to a flow in approximate hydrostatic equilibrium, with a mean radial velocity that is highly subsonic at $r \gtrsim$ a few r_g (see Fig. 14). Figure 13 also shows that the density of the flow in the inner region is much lower in the simulations with heating than in the initial solution. This is consistent with accretion rate being $\ll \dot{M}_B$ (Fig. 10).

In Figures 12-14 we have presented results averaging over the full range of θ , from $\theta = 0$ to $\theta = \pi$. However, the initially vertical magnetic field lines impose an asymmetry on the flow so that the flow profiles are not spherically symmetric. As seen in Figure 16 (discussed below), the temperature is larger in the equatorial region compared to the pole, by roughly a factor of 10 at small radii; the same is true for the density. The equatorial region is primarily gas pressure dominated while the poles are magnetically dominated. The relative importance of the different energy transport mechanisms (shown in Fig. 12) also varies with angle; in particular, conduction dominates at the poles (and averaged over all angles), but is less important in the equatorial region where the field lines are less ordered. Overall, the angular asymmetry we find in these nonrotating simulations is not as large as in simulations with significant angular momentum (e.g., Hawley & Balbus 2002) which show “funnels” with radial outflows. In our spherical simulations, the time averaged flow is always inwards at all angles (although there can be outflow at certain times; see Fig. 16).

Although there are modest quantitative differences between the simulations with anisotropic conduction and those without (Figs. 10-14), our results demonstrate that many of the properties of magnetized spherical accretion are in fact rather similar in the two cases. An important difference, however, is that for even modest thermal conductivities ($\alpha_c \sim 0.2$; eq. [7]), conduction is the dominant mechanism of energy transport and transports a significant fraction of the energy released by magnetic dissipation to large radii (Fig. 11 & 12). By contrast, in the MHD simulations without conduction, we find that the net energy transport is *inwards*. Although convective motions are present, the convective luminosity is much smaller than $G\dot{M}M/(r - r_g)$ at all radii.

An additional interesting difference between the simulations with and without conduction is the “flaring” in the simulations with anisotropic conduction (Fig. 10-11). The accretion rate, resistive heating, and conduction luminosity all show regular rapid increases (“flares”) by a factor of $\sim 10 - 100$ on a timescale ~ 10 orbital periods at $\sim r_{\text{in}}$ (see Fig. 15). The characteristic timescale between such flares is a fraction of an orbital period at r_{out} . The flare timescales do not depend sensitively on the value of the thermal conductivity, as long as $\alpha \simeq 2$. As shown in Fig. 10, flares are most prominent for run S2, the run with the smallest mass accretion rate among $r \ll r_B$ simulations (see Table 2).

To assess the robustness of this flaring, we performed several checks. Similar flaring is much less pronounced in the MHD simulations and in simulations with an isotropic thermal conductivity, even though the reduction in \dot{M} rel-

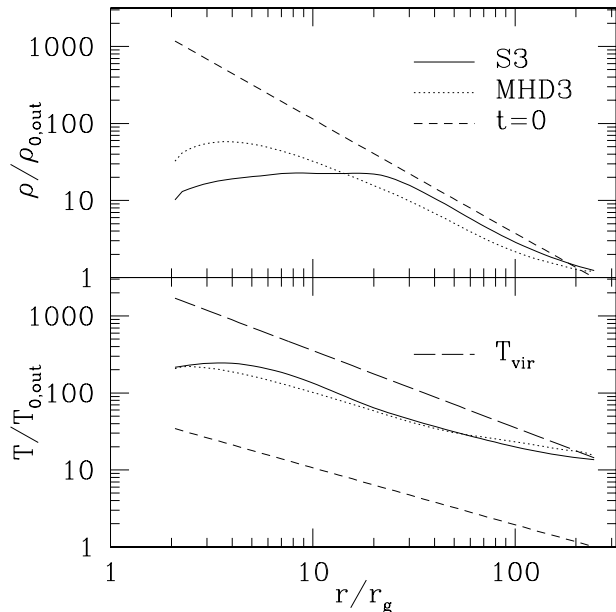


Figure 13. Time and angle averaged density (upper panel) and temperature (lower panel) as a function of radius for S3 ($\alpha_c = 2$) and MHD3 compared to the initial solutions; the profiles for S3 and MHD3 are angle and time-averaged. In both S3 & MHD3, the plasma is heated to nearly the virial temperature and the density in the inner part of the flow decreases significantly. As shown in Fig. 16, there is a significant asymmetry between the polar and equatorial regions; the density and temperature are larger at the equator while magnetic pressure dominates at the poles.

ative to \dot{M}_B is similar; in addition, the flaring is more pronounced for larger values of α_c . To assess whether the flaring is a numerical artifact, we carried out simulations implementing anisotropic conduction using the method of Parrish & Stone (2005) and Sharma et al. (2006), which uses simple finite differencing (our method, based on Sharma & Hammett 2007, limits the heat fluxes so that the temperature is always positive). We find quite similar flaring with the two methods.³ We also changed the magnitude of the artificial viscosity and the explicit resistivity, and the form of the explicit resistivity (e.g., $\eta \propto dr(c_s^2 + V_A^2)^{1/2}$ instead of eq. 6, where c_s and V_A are the local isothermal sound speed and Alfvén speed, respectively), but the flaring in run S3 (Fig. 10) persisted. These checks argue against the flaring being a numerical artifact. The physical origin of this flaring is, however, not clear. The MTI could in principle be present because the inflow is subsonic, but it should be stabilized by magnetic tension. The flaring we find is qualitatively similar to the “relaxation oscillations” seen in some 1D time-dependent models of spherical accretion with radiative heating (e.g., Cowie et al. 1978) and could be analogous, with spatially extended heating and redistribution of

³ At late times in the simulations with conduction implemented using simple finite differencing, the temperature can become negative, which demonstrates the importance of using a method that guarantees that heat flows from hot to cold, such as that of Sharma & Hammett (2007).

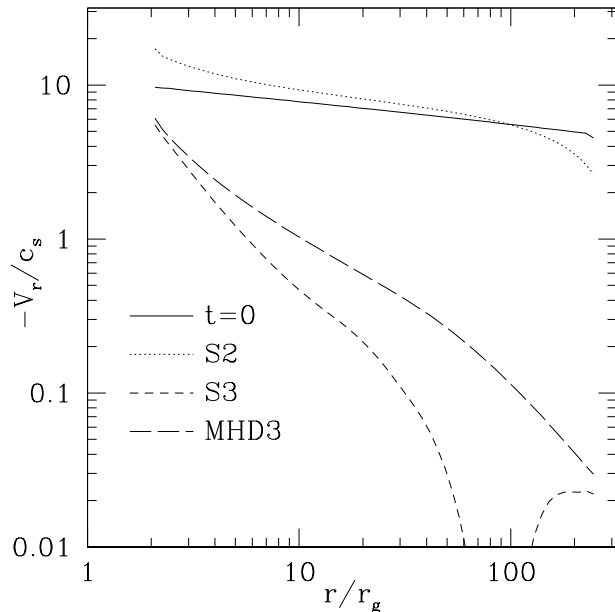


Figure 14. The ratio of the time and angle averaged Mach number (radial velocity divided by isothermal sound speed c_s) at late times as a function of radius for the initial Bondi solution (solid line), S2 (dotted line), S3 (short dashed line), and MHD3 (long-dashed line). For the calculations with significant magnetic dissipation (S3 & MHD3), the average infall speed is subsonic at $r \gtrsim$ few r_g , and the plasma is in rough hydrostatic equilibrium. Although not shown, we find that the radial infall velocity in the polar regions is larger than in the hotter equatorial regions.

energy by anisotropic conduction precluding the existence of a steady state solution.

Figure 15 shows a number of quantities characterizing one of the accretion/heating flares over a small interval in time. The gravitational potential energy released by accretion ($GMM_{\text{in}}/r_{\text{in}}$) peaks slightly earlier in time than the volume integrated resistive heating rate (H_{res}); this is consistent with the field being amplified by flux freezing and then dissipated by resistive diffusion. Figure 15 also shows the maximum values of the local resistive heating rate (ηJ^2), the internal energy per unit volume (e), and the temperature, and the minimum value of the density (where the maximum/minimum are over all grid cells in the computational domain). The maximum resistive heating rate and maximum internal energy have a time-dependence similar to that of the accretion energy. The peak temperature and minimum density, on the other hand, occur after the majority of the resistive heating has taken place, and their evolution in time is much more rapid. In fact, the increase in temperature (decrease in density) occurs on a timescale comparable to the free-fall timescale at small radii.

Figure 16 shows contour plots of temperature relative to the virial temperature and local resistive heating rate (in arbitrary units) in the inner $15r_g$ at the time of the peak in $\max[T]$ in Figure 15 ($\Omega_{\text{in}}t \simeq 510$). Also shown are the velocity unit vectors. The resistive heating is strongly concentrated in the equatorial region at $\lesssim 5r_g$ (near the sonic point; see Fig. [14]) where rapid inflow brings together oppositely directed field lines. Strong heating leads to modestly

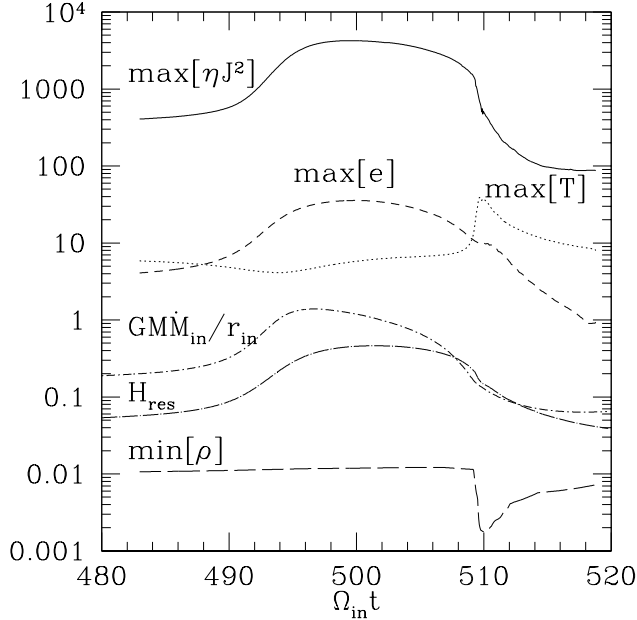


Figure 15. Zoom-in on the time-dependence of an accretion/heating flare for run S3; note that time here is in units of $\Omega_{in}^{-1} \equiv (GM/r_{in}^3)^{-1/2}$ not Ω_{out}^{-1} . The maximum values of the resistive heating rate (ηJ^2), internal energy per unit volume (e), and temperature (T), along with the minimum value of the density (ρ), the energy released by accretion (GMM_{in}/r_{in}), and the volume integrated resistive heating rate (H_{res}) are all shown as a function of time (the $\max[X]$ and $\min[X]$ are taken over all grid points in the computational domain). All quantities are in arbitrary units. As shown in Figure 16, the peaks in temperature, heating rate, etc. occur at small radii near the equatorial plane.

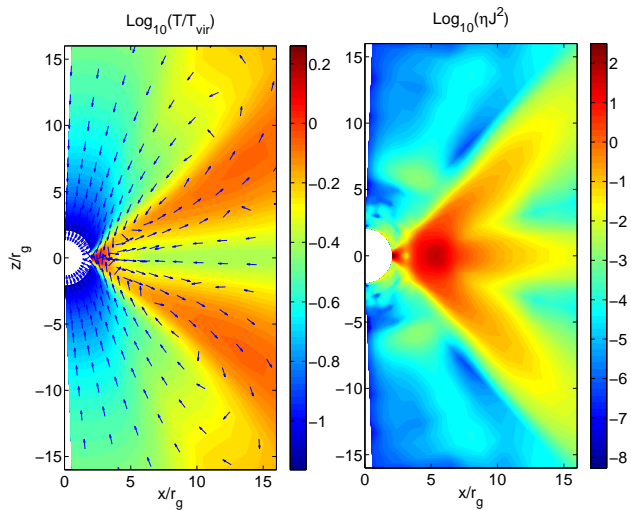


Figure 16. *Left:* Log_{10} of plasma temperature normalized to the virial temperature (T/T_{vir}) in the inner $15 r_g$ for run S3 at $\Omega_{int} = 510$ (the peak in $\max[T]$ in Fig. 15). Arrows show the direction of the *velocity* vectors. *Right:* Log_{10} of the local resistive heating rate, ηJ^2 (in arbitrary units), at the same time. Both the resistive heating and temperature peak at small radii in the equatorial region.

supervirial temperatures at small radii. This energy diffuses to large radii along a finite set of field lines because of the anisotropic nature of conduction. The supervirial temperatures also reverse the inflow along particular field lines, leading to a weak mass outflow (as shown by the velocity unit vectors in Fig. 16).

5 DISCUSSION

We have studied the effects of anisotropic thermal conduction on the dynamics of spherical accretion flows using global axisymmetric simulations. Our simulations address two different physical effects that operate on different radial scales in spherical accretion flows.

5.1 The MTI in Spherical Accretion Flows

We have calculated the nonlinear saturation of the magnetothermal instability (MTI) at radii $\sim r_B$ in spherical accretion flows (§3), where $r_B \simeq GM/c_s^2$ is the gravitational sphere of influence of the central object (of mass M) and c_s is the isothermal sound speed of the ambient plasma. The MTI does not grow appreciably at radii $\ll r_B$ for the canonical Bondi spherical accretion solution because the inflow is supersonic. Our simulations are the first global simulations of the MTI, but our results are largely consistent with the previous local simulations of Parrish & Stone (2005, 2007). We have focused on studying the saturation of the MTI for initially weak vertical magnetic fields ($\beta \gg 1$).

We find that the MTI saturates by aligning the magnetic field lines with the temperature gradient, i.e., by making the field lines primarily radial (Figs. 2 - 4). This occurs on approximately the local dynamical time ($\sim [g|d\ln T/dz|]^{-1/2}$). Since the field lines end up largely radial, the rearrangement of the magnetic field results in a radial heat flux similar to the field-free (Spitzer) value; in the saturated state, energy transport by conduction dominates transport by the convective motions associated with the MTI (Fig. 7). Given the significant radial heat flux, the density and temperature profiles of the accretion flow adjust to satisfy $\nabla \cdot \mathbf{Q} \simeq 0$, where \mathbf{Q} is the conductive flux of energy. In all cases of $\kappa(r)$ that we considered (see §2.1), the mass accretion rate in the presence of the MTI differs only modestly from the canonical Bondi rate (Fig. 6).

Our results indicate that the saturation of the MTI is quasilinear in the weak field limit: the magnetic and convective energy densities in the saturated state are roughly proportional to the initial magnetic energy density (Fig. 8).⁴ The net result is that the MTI amplifies the magnetic field by a factor of $\sim 10 - 30$ independent of the initial magnetic field strength (for weak fields). For stronger initial fields, magnetic tension can saturate the MTI before the field has become largely radial (Parrish & Stone 2005, 2007). In this case, the amplification of the magnetic field will be less than we have found here.

The quasilinear saturation of the MTI can be understood qualitatively using linear theory (Quataert 2008); as

⁴ Ian Parrish has found this same result in local three-dimensional Cartesian simulations (private communication).

a result, we believe that this is a general property of the MTI, rather than being specific to the spherical accretion problem considered in this paper. The linear growth rate of the MTI is reduced by a factor of $\sim B_\theta/B$ for nearly radial fields, and the growth occurs on progressively smaller scales for small B_θ/B (eq. [8]). Thus, as the field lines become radial, the MTI effectively shuts off its own growth. This is in stark contrast to the magnetorotational instability in differentially rotating plasmas, which is an exact nonlinear solution of incompressible MHD, and for which growth continues unimpeded even when $\delta B \gg B$ (Goodman & Xu 1994).

One simplification in the current calculations is that we have not included anisotropic viscosity; the diffusion coefficient for anisotropic viscosity in a collisional plasma is smaller than the diffusion coefficient for anisotropic conduction by a factor of $\sim (m_p/m_e)^{1/2} \simeq 40$; in a collisionless plasma, the relative importance of these two effects is more complex and depends on small-scale kinetic microinstabilities (e.g., Sharma et al. 2007). Local simulations of the MRI find that the saturation of the instability is sensitive to the ratio of the resistivity to the viscosity (e.g., Fromang et al. 2007). In future calculations, the effects of anisotropic viscosity on the evolution of the MTI should thus be studied, but this is probably first best done in a local calculation, rather than in the global geometry considered here.

5.1.1 Application to the Galactic Center

One potential application of the MTI at large radii in spherical accretion flows is to the observed Faraday rotation from the Galactic center. Millimeter observations of Sgr A* find a rotation measure (RM) of $\simeq -6 \times 10^5 \text{ rad m}^{-2}$ that has been roughly constant over the past ~ 8 years (Aitken et al. 2000; Bower et al. 2005; Marrone et al. 2007). Propagation through the interstellar medium cannot account for this large RM. In addition, X-ray observations of the thermal plasma in the central parsec of the Galactic center find that the electron number density is $\approx 100 \text{ cm}^{-3}$ and the temperature is $\approx 2 \text{ keV}$ at a distance of $\approx 10^5 r_g$ from the black hole (Baganoff et al. 2003; Quataert 2004). If the magnetic field on this scale were uniform, radial, and in rough equipartition with the thermal pressure, $B \approx 2\beta^{-1/2} \text{ mG}$ and $RM \approx 5000\beta^{-1/2} \text{ rad m}^{-2}$, two orders of magnitude smaller than what is observed. This shows that the observed RM must be produced at distances $\ll 10^5 r_g$ from Sgr A*.

Our calculations show that given a sufficiently coherent seed magnetic field at large radii, the MTI will generate a relatively coherent radial field at distances of $\sim r_B \sim 10^5 r_g$ from Sgr A*. Given the measured density and temperature of the plasma, the electron mean free path is $\sim r_B$ at radii $\sim r_B$ and thus the MTI grows on a dynamical time. Numerical simulations of accretion onto Sgr A* from stellar winds located at $\sim 10^5 - 10^6 r_g$ find that the circularization radius of the flow is $r_{\text{circ}} \sim 10^3 - 10^4 r_g$ (Cuadra et al. 2006). If the Bondi solution is applicable from the scale of the observed plasma at $\sim r_B$ to $\sim r_{\text{circ}}$, then $dRM/d \ln r \propto r^{-7/4}$ at fixed β and the RM produced by the roughly spherical inflowing plasma at large radii around Sgr A* is

$$RM \sim 10^7 \beta^{-1/2} \left(\frac{r_{\text{circ}}}{10^3 r_g} \right)^{-7/4} \text{ rad m}^{-2}. \quad (13)$$

It is difficult to determine with confidence whether the stellar winds feeding Sgr A* – or the shocks between such winds – produce a sufficiently large and coherent ‘seed’ magnetic field at $\sim r_B$ to account for the RM towards Sgr A*. However, for an initial value of β of β_0 (assumed $\gg 1$) at $r_B \sim 10^5 r_g$, the combined action of the MTI and flux freezing will decrease β to $\sim 10^{-6} \beta_0 (r_{\text{circ}}/10^3 r_g)^{-3/2}$ at r_{circ} . Thus even a relatively weak magnetic field ($\beta_0 \sim 10^6 - 10^8$; $B_0 \sim 0.1 - 1 \mu\text{G}$) on scales of $\sim 10^5 r_g \sim 0.1 \text{ pc}$ will be amplified by the MTI and flux freezing to a value capable of explaining the observed RM from Sgr A*.⁵ Our explanation for the observed RM also naturally accounts for its stability, since the dynamical time at $\sim 10^3 - 10^4 r_g$ is $\sim 0.3 - 10$ years. By contrast, if the RM is produced in the rotating accretion flow even closer to the black hole, it is harder to account for the observed stability (Sharma, Quataert, & Stone 2007).

5.2 The Effects of Thermal Conduction on the Dynamics of Spherical Accretion

The second set of simulations we have carried out address the effects of anisotropic conduction and resistive dissipation of magnetic energy on the dynamics of spherical accretion flows at small radii $\sim 2 - 256 r_g$ (§4). Our results are in reasonable agreement with those of Igumenshchev & Narayan (2002), who studied the same physical problem but without anisotropic conduction. Although the MTI does not dramatically modify the dynamics of spherical accretion at $\sim r_B$, it does generate a significant radial magnetic field that can be further amplified by flux freezing. For $r \ll r_B$, supersonic inflow in (magneto)hydrodynamic Bondi accretion leads to magnetic field amplification by flux freezing, converging field lines, and resistive heating of the plasma. When the magnetic energy density is comparable to the gravitational energy density, resistive heating can heat the plasma up to the virial temperature and significantly modify the dynamics of spherical accretion (Igumenshchev & Narayan 2002). This is only likely to occur for sub-Eddington accretion rates onto compact objects, since only under these conditions is radiative cooling negligible.

All of our calculations with resistivity and strong magnetic fields at $\sim 100 r_g$ – both with and without anisotropic conduction – show a significant decrease in \dot{M} after a few free-fall times, with $\dot{M} \sim 0.01 \dot{M}_B$ in the quasi steady state at late times (Fig. 10). The high temperatures generated by resistive heating stifle the inflow, reducing the accretion rate (Fig. 10) and generating a subsonic (Fig. 14) nearly hydrostatic atmosphere around the central object. For realistic values of the thermal conductivity for collisionless plasmas (see §2.1), we find that conduction transports the majority of the energy released by accretion to large radii (Figs. 11 & 12). By contrast, although turbulent motions are present, there is no net convective energy flux from small to large radii, even in our simulations *without* conduction (Fig. 12).⁶ This indicates that significant radial transport of energy (be

⁵ If most O stars have surface magnetic fields comparable to the $\sim \text{kG}$ field measured in the young O star θ^1 Orinis C (Donati et al. 2002), stellar winds alone will fill the central $\sim 0.1 \text{ pc}$ with a magnetic field $\sim \text{mG}$.

⁶ Our interpretation of the MHD simulations of spherical accretion without conduction thus differs from that of

it conductive or convective) is not necessary to suppress accretion onto the central object; instead, heating that raises the temperature to the virial temperature appears sufficient. Indeed, it is well-known that there is no supersonic Bondi solution for adiabatic indices $\gamma > 5/3$. Heating via resistive dissipation and/or artificial/numerical viscosity effectively increases the adiabatic index above this value, thus stifling accretion onto the central object. Thermal conduction can further reduce the accretion rate by conducting the dissipated energy to larger radii.

Overall, our results are in reasonable agreement with Johnson & Quataert (2007)'s simplified one-dimensional models for the structure of spherical accretion in the presence of conduction and plasma heating. Our simulations confirm their hypothesis that a significant fraction of the energy released by accretion is transported to large radii by thermal conduction. In addition, their prediction that \dot{M}/\dot{M}_B should decrease by $\simeq 2 - 3$ orders of magnitude – with a factor of ~ 10 suppression due to heating alone (their Fig. 8) – is consistent with our numerical results.

The reduction in \dot{M} that we find is similar to that needed to explain the low luminosity of Sgr A* (e.g., Sharma, Quataert, & Stone 2007). It is also reasonably consistent with the limits on \dot{M} from Faraday rotation measurements (e.g., Marrone et al. 2007). However, it is unlikely that the present calculations are quantitatively applicable to Sgr A* given the estimated circularization radius of the accretion flow in Sgr A* of $r_{\text{circ}} \sim 10^3 - 10^4 r_g$ (Cuadra et al. 2006). The gravitational potential energy released accreting to $\sim r_{\text{circ}}$ is unlikely to significantly modify the accretion flow dynamics. Thus the accretion rate and outward conductive energy flux will be largely determined in the rotationally supported flow at radii $\lesssim r_{\text{circ}}$. Nonetheless, our results demonstrate that even in the absence of angular momentum, the Bondi accretion solution does not apply to dilute magnetized accretion flows. Instead, the accretion flow is heated to nearly the virial temperature by resistive dissipation of magnetic energy, the accretion rate is $\ll \dot{M}_B$, and most of the gravitational potential energy released by accretion is transported to large radii by thermal conduction. In addition, in our simulations with anisotropic conduction, the accretion and heating are time-dependent, with episodic “flaring” (Figs. 10-11) followed by mass outflow along a subset of the field lines (Fig. 16). It is important to determine if analogous effects are present in rotating accretion flows (which is by no means clear), given the possible application to the broad-band electromagnetic flares observed from Sgr A* (e.g., Marrone et al. 2008) and other systems.

5.3 Additional Applications

In addition to the applications considered here, thermal conduction is also important in the intracluster medium of galaxy clusters (Sarazin 1986). A conductive energy flux from the accretion flow onto the central black hole in the nucleus of galaxy clusters could help heat the intercluster plasma at radii $\sim 0.1 - 1$ kpc and prevent it from

cooling catastrophically. At larger radii, the temperature in clusters increases from $r_B \sim 0.1$ kpc to ~ 100 kpc, where it begins to decrease (Piffaretti et al. 2005). Thus the plasma at intermediate radii in clusters appears stable to the MTI (it is, however, unstable to the HBI; Quataert 2008; Parrish & Quataert 2008). However, Chandran & Dennis (2006) have shown that cosmic rays from a central active galactic nucleus (AGN) can make the plasma in the cores of clusters unstable to a cosmic-ray mediated version of the MTI if $dp_{CR}/dr + nkdT/dr < 0$ (p_{CR} is the cosmic ray pressure), i.e., if there is a sufficiently large cosmic ray flux from the central AGN. It is likely that the MTI in the presence of cosmic rays saturates in a manner analogous to that found here, by aligning the field lines primarily in the radial direction, with a roughly constant radial cosmic ray and conductive luminosity. One of the outcomes of this work (see also Parrish & Stone 2007) is that convective transport of energy is subdominant in the presence of the MTI; this may rule out turbulent heating due to cosmic-ray driven convection (Chandran & Rasera 2007) as an important source of plasma heating in cluster cores. However, if the cosmic-ray mediated MTI generates a largely radial magnetic field in cluster cores, the conductive energy flux from large radii can produce significant heating at small radii, analogous to what we have found in our global simulations (see Fig. [7]). It is clear that a careful study of the combined action of the MTI and HBI in the presence of cosmic-rays is necessary to understand the thermal structure of galaxy clusters.

ACKNOWLEDGMENTS

We thank Bryan Johnson and Ian Parrish for useful discussions. We thank the referee Steve Balbus for detailed comments. PS and EQ were supported in part by NASA grant NNG06GI68G and the David and Lucile Packard Foundation. PS was partly supported by DOE award DE-FC02-06ER41453 to Jon Arons. JS was supported by DOE grant DE-FG52-06NA26217. This research used resources of the National Energy Research Scientific Computing Center, which is supported by the Office of Science of the U.S. Department of Energy under Contract No. DE-AC02-05CH11231. Computational resources were also provided by the Princeton Plasma Physics Laboratory Scientific Computing Cluster. Part of the code was tested with the Tungsten cluster at the National Center for Supercomputing Applications at the University of Illinois at Urbana-Champaign.

REFERENCES

- Aitken, D. K. et al. 2000, *ApJ*, 534, L173
 Baganoff, F. K. et al. 2003, *ApJ*, 591, 891
 Balbus, S. A. & Hawley, J. F. 1998, *Rev. Mod. Phys.*, 70, 1
 Balbus, S. A. 2000, *ApJ*, 534, 420
 Bondi, H., 1952, *MNRAS*, 112, 195
 Bower, G. C. et. al. 2005, *ApJ*, 618, 29
 Braginskii, S. I. 1965, *Reviews of Plasma Physics*, v. 1, p. 205, Consultants Bureau
 Chandran, B. D. G. & Dennis, T. J. 2006, *ApJ*, 642, 140

Igumenshchev & Narayan (2002), who emphasized the importance of radial energy transport by convection. This needs to be investigated further.

- Chandran, B. D. G. & Rasera, Y. 2007, arXiv:0707.2351
- Cowie, L. L. & McKee, C. F. 1977, ApJ, 211, 135
- Cowie, L. L., Ostriker, J. P., & Stark, A. A. 1978, ApJ, 226, 1041
- Cuadra, J., Nayakshin, S., Springel, V., & di Matteo, T. 2006, MNRAS, 366, 358
- Donati, J.-F., Babel, J., Harries, T. J., Howarth, I. D., Petit, P., & Semel, M. 2002, MNRAS, 333, 55
- Fleming, T. P., Stone, J. M., & Hawley, J. F. 2000, ApJ, 530, 464
- Fromang, S., Papaloizou, J., Lesur, G., & Heinemann, T. 2007, A&A, 476, 1123
- Goodman, J., & Xu, G. 1994, ApJ, 432, 213
- Hawley, J. F. & Balbus, S. A. 2002, ApJ, 573, 738
- Igumenshchev, I. V. & Narayan, R. 2002, ApJ, 566, 137
- Johnson, B. M. & Quataert, E. 2007, ApJ, 660, 1273
- Marrone, D. P. et al. 2007, ApJ, 654, L57
- Marrone, D. P. et al. 2008, ApJsubmitted, arXiv:0712.2877
- Paczynski, B. & Wiita, J. 1980, A&A, 88, 23
- Parrish, I. J. & Stone, J. M. 2005, ApJ, 633, 334
- Parrish, I. J. & Stone, J. M. 2007, ApJ, 664, 135
- Parrish, I. J. & Quataert, E. 2008, ApJ, in press
- Piffaretti, R., Jetzer, P., Kaastra, J. S., & Tamura, T. 2005, A&A, 433, 101
- Quataert, E. 2003, Astron. Nachr., 324, 435
- Quataert, E. 2004, ApJ, 613, 322
- Quataert, E. 2008, ApJ, 673, 758
- Rees, M. J. et al. 1982, Nature, 295, 17
- Sarazin, C. L. 1986, Rev. Mod. Phys., 58, 1
- Shvartsman, V. F., 1971, Soviet Astron., 15, 377
- Sharma, P., Hammett, G. W., Quataert, E., & Stone, J. M., 2006, ApJ, 637, 952
- Sharma, P., Quataert, E., Hammett, G. W., & Stone, J. M. 2007, ApJ, 667, 714
- Sharma, P., Quataert, E., & Stone, J. M. 2007, ApJ, 671, 1696
- Sharma, P. & Hammett, G. W. 2007, J. Comp. Phys., 227, 123
- Snyder, P. B., Hammett, G. W., & Dorland, W. 1997, Phys. Plasmas, 4, 3974
- Spitzer, L. 1962, Physics of Fully Ionized Gases (New York: Wiley Interscience)
- Stone, J. M., Norman, M. L. 1992a, ApJS, 80, 753
- Stone, J. M., Norman, M. L. 1992b, ApJS, 80, 819
- Stone, J. M. & Pringle J. E. 2001, MNRAS, 322, 461
- Tanaka, T. & Menou, K. 2006, ApJ, 649, 345